Nanoscale

PAPER

View Article Online
View Journal | View Issue

Cite this: *Nanoscale*, 2014, **6**, 3289

Non-wrinkled, highly stretchable piezoelectric devices by electrohydrodynamic direct-writing†

YongQing Duan, YongAn Huang,* ZhouPing Yin,* NingBin Bu and WenTao Dong

Received 12th November 2013
Accepted 16th December 2013

DOI: 10.1039/c3nr06007a

www.rsc.org/nanoscale

Piezoelectric structures, in forms that allow mere in-surface deformations under large strains, are attractive for bio-integrated systems. Here, mechano-electrospinning (MES) is presented to direct-write straight nanofibers of polyvinylidene fluoride onto a prestrained poly(dimethylsiloxane) (PDMS) substrate, to position and polarize a piezoelectric nanofiber array in one-step. Wrinkled/non-wrinkled buckling modes are found when the substrates are released, and the morphology of the direct-written fiber proved the key to determine the buckling modes, which can be tuned precisely by MES parameters. The non-wrinkled, stretchable piezoelectric devices with a highly synchronized serpentine fiber array exhibit their in-surface deformation and stable piezoelectric performance up the failure strain of PDMS (~110% in our study), which may be used as stretchable sensors and energy converters/providers.

Introduction

Development of stretchable electronics that offer elastic responses to large strain ($\gg 1\%$) deformations has accelerated in recent years for a range of new applications, such as sensitive cyber skins,[1,2] epidermal health monitors[3] or motion detectors,[4] and hemispherical electronic eye cameras.[5] Of particular importance are the stretchability of the energy conversion/supply devices,[6,7] to allow for direct and natural integration with the stretchable electronics. Percolation networks[8,9] and continuous wavy structures[3,10] are the two typical architectures to realize high stretchability. For wavy structures, buckled,[10–12] serpentine[13,14] and self-similar structures[6] have been recently considered as the dominating designs, and the stretchability depends largely on out-of-surface buckling or wrinkling. However, stiff and out-of-surface buckled structures lead to non-conformal contacts, thicker encapsulation layers and decreased bio-compatibility. Stretchable electronic devices that directly interface with the human body or artificial skin accelerate the designs with both large stretchability, lightweight construction, easy encapsulation and high compatibility. In-surface buckled nanowires[15–17] can meet these requirements but many kinds of nanowires generated through chemical growth like silicon nanowires[18] have complex and expensive fabrication, poor positioning performance and inflexible fiber morphology. Thus, producing a stretchable energy provider with in-surface buckled structures in a simple and controllable manner is critical. Piezoelectric materials can produce electric power and signals when subject to mechanical deformation,[19,20] which is very suitable for converting/supplying energy in strain-driven occasions. Previous stretchable piezoelectric devices are usually fabricated using stiff inorganic nanoribbons with out-of-surface buckled structures, which are first produced by techniques like lithography and then transferred onto pre-strained substrates.[7,21] The multi-step manufacturing process is low-efficiency, expensive, complex, and incompatible with elastomeric substrates. Piezoelectric polyvinylidine fluoride (PVDF), with attractive piezoelectric effect and solution-processability, has been widely applied in pressure sensor,[19,22] energy generator,[20] *etc.* PVDF in the form of straight fiber and planar thin film cannot be stretched, thus they are unable to be integrated into stretchable electronics. Additionally, achieving high-performance PVDF requires poling to realize maximum polarization, which requires multiple preparatory or post-processing steps.[23] It is challenging to produce in-surface buckled PVDF fibers with a high piezoelectric response in a simple and cost-effective fabrication process.

Here, mechano-electrospinning (MES)[24,25] is first proposed to fabricate large-area, high performance stretchable piezoelectric nanowire devices without out-of-surface buckling or wrinkling. The key is to direct-write PVDF nanofibers onto a prestrained elastomeric substrate, to form in-surface buckled fibers in a controllable manner. The biggest difference between MES and near-field electrospinning[26]/traditional electrospinning[27] is MES has a high speed motion platform, which exerts a large dragging force on the fiber to help achieve positioning. MES pulls the fluid through an electric force and a mechanical drawing force simultaneously, in a wide range of distances,[25] and is compatible with many soft materials.[28,29] MES has superior advantages for fabricating stretchable piezoelectric devices. (i) MES is able to direct-write PVDF fibers on elastomers

State Key Laboratory of Digital Manufacturing Equipment and Technology, Huazhong University of Science and Technology, Wuhan 430074, People's Republic of China. E-mail: yahuang@hust.edu.cn; yinzhp@mail.hust.edu.cn

† Electronic supplementary information (ESI) available. See DOI: 10.1039/c3nr06007a

and transfer the nonpolar phase (α, γ) into the polar phase (β) in one step.[30] MES can precisely direct-write nanofibers since the relatively large mechanical drawing force can overcome the electric repulsion resulted from the insulated elastomer substrate.[31] Meanwhile, the applied electric field naturally causes local poling of PVDF by making the dipole moments to all point at the same direction, thus enabling piezoelectric properties. (ii) MES is able to form in-/out-of-surface buckling in a controllable manner, since it can tune the morphology of the electrospun fibers from a ribbon to a cylinder by adjusting the process parameters, such as nozzle-to-substrate distance,[25] solution density and temperature. Highly uniform in-surface buckled fibers satisfy the requirements of high compatibility and easy encapsulation. (iii) MES is a kind of high-speed and large-area digital printing, which can direct-write fibers with precise positioning, controllable morphology and tunable direct-writing resolution, onto a large-area substrate and even flexible web *via* a roll-to-roll technique.[32] Stretchable piezoelectric devices are built by establishing electrical contacts to the ends of the aligned buckled fibers. The reciprocating stretch-release tests show that these devices are of high electrical and mechanical performance (up the failure strain of PDMS, ~110% in our study).

Experimental

Preparation of PVDF solution and PDMS substrate

PVDF (Kynar 761) was purchased from Arkema Investment Co. Ltd and used as received. A total of 3.6 g PVDF was dissolved in a mixture of 8.2 mL DMF and 8.2 mL acetone and heated at 40 °C for 4 h to make the solution homogeneous. The PDMS substrate (Sylgard 184, Dow Corning, Inc.) with a thickness of 1 mm was prepared by mixing the base and the curing agent with a ratio of 10 : 1. The mixture was first placed in a vacuum oven to remove air bubbles and then thermally cured at 70 °C for 50 min. The substrate used was fresh and sticky.

Electrospinning of PVDF nanofibers

The PVDF solution was delivered using a syringe pump (11 Pico Plus, HARVARD, Inc.) at a feed rate of 600 nL min^{-1}. A stainless steel nozzle (inner diameter 260 μm and external diameter 510 μm) was adopted as an electrode, and the ground collector was a metal plate fixed on a moving stage. A tensile platform was fixed on the collector to prestretch the PDMS substrate. A high voltage was exerted between the nozzle and the collector to generate a Taylor cone and assist to pull out the jet through a current power supplier (DW-P403, Dongwen Inc.). The applied voltage was 1.5 kV, the nozzle-to-collector distance varied from 4 to 10 mm to tune the fiber cross-section shape from ribbon to circle, and the moving speed of the substrate was adjusted from 200 to 400 mm min^{-1}.

Characterization

The electrospun nanofibers were examined with laser scanning confocal microscopy (LSCM, KEYENCE VK-X200K). The fiber diameter and cross-section were obtained from LSCM images *via* image analysis software VK-X Series. The morphological analysis was performed by scanning electron microscopy (SEM) with a Sirion 200 system (FEI). The electric properties of the buckled PVDF fibers were obtained through a semiconductor characterization system (KEITHLEY 4200-SCS) and probe system (CASCADE SUMMTI 11000).

Device fabrication and measurements

PDMS substrates with buckled PVDF fibers (100% prestrain) were fixed on a custom-built tensile platform, the length between the two electrodes was 3 cm, and the electric connections were established with copper films (50 μm thick). Current/voltage measurements were performed with a probe system (CASCADE SUMMTI 11000) and a semiconductor parameter analyzer (KEITHLEY 4200-SCS). Signals were not amplified before acquisition. All measurements were performed at 20 °C.

Results and discussions

PVDF fibers were direct-written onto a prestrained PDMS substrate through MES, to obtain high uniform in-surface or out-of-surface buckled fibers for making stretchable devices. This approach contains three key steps: prestraining the elastomeric substrate, direct-writing of straight fibers, and releasing the prestrained substrate (Fig. 1a). The biggest challenge lies in the direct-writing that the jetted fiber is positioned on the prestrained substrate precisely with a specific cross-section and tunable resolution (Fig. 1b). Fig. 1c and d show direct-written parallel and latticed PVDF fibers on PDMS substrates. These precisely positioned, straight and uniform fibers benefit from a combination of the electric field force and mechanical drawing

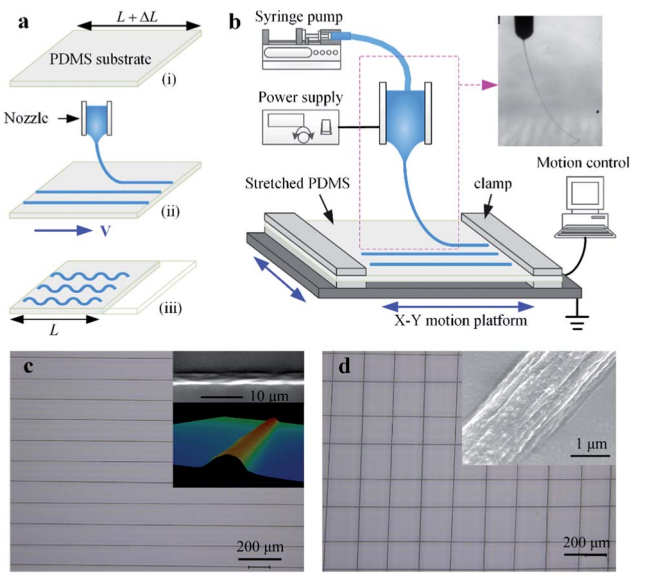

Fig. 1 (a) Three steps for directly fabricating buckled fibers: (i) prestraining the elastomeric substrate, (ii) direct-writing straight fibers on the prestrained substrate, (iii) releasing the prestrained substrate, and buckled fibers appear. (b) Schematic diagram of MES. (c) Parallel and (d) latticed fibers on PDMS substrates. Inset SEM/LSCM images show the morphology of a single PVDF fiber.

force (Fig. S1†). MES can produce large-area ordered fibers as long as the collector is continuously conveyed by the motion stage or roll-to-roll system. The insets are SEM and 3D LSCM images of a straight fiber on the PDMS substrate. Based on MES, the sectional area and shape (the width and height) of the fiber are tunable *via* changing process parameters like voltage, speed and nozzle-to-collector distance (Fig. S2†).

The PVDF fibers buckle under compressive strain when the prestrained substrate is released, and the buckling behavior is affected by fiber section morphology which is controlled by the MES process parameters like the nozzle-to-collector distance. There are two buckling modes observed in our experiments (Fig. 2), out-of-surface buckling (normal-to-surface or incline-to-surface buckling) and in-surface buckling. In incline-to-surface buckling, the fiber is inclined rather than perpendicular to the substrate. As the materials of the fiber/substrate and the thickness/prestrain of substrate are given, the buckling behavior of the fibers can only be determined by their section morphology which is controlled by the MES process parameters (Fig. S2†). In MES, the nozzle-to-collector distance is tunable, which can be used to determine the solidification degree of the jetting fiber and thus adopted to control the fiber morphology (the cross-sectional shape and size).[25] The liquid fiber spreads into a flat ribbon when it reaches the elastomeric substrate, and then the ribbon tends to buckle normal to the substrate (Fig. 2a). When the nozzle-to-collector distance is increased from 6 to 8 mm, the fiber deposited onto the substrate prefers a semi-solid state. The direct-written ribbon tends to have a high aspect ratio, and incline-to-surface buckling usually happens (Fig. 2b). Incline-to-surface buckling is a transitional phase from normal-to-surface to in-surface buckling, and we will prove it theoretically. When the distance further increases, the jetting fiber completely solidifies in air, and the deposited fiber has an almost circular cross-section (Fig. 2c). Under this case, the fiber-on-substrate structure tends to form in-surface buckling. With the increase of the nozzle-to-collector distance, the state of the fiber changes from liquid to semi-solid and finally to solid when the fiber contacts the substrate, and thus the aspect ratio of the direct-written fiber increases gradually.

The electrospun fibers on a prestrained substrate will form normal-to-surface/incline-to-surface/in-surface buckling when the prestrain of the substrate is released. In-surface/normal-to-surface buckling can be fabricated by transferring nanowires[15] or inorganic ribbons[33] onto prestrained substrates. Nanowires and inorganic ribbons are fabricated by two different processes, so their buckling modes are difficult to be tuned dynamically.

In order to validate the influence of fiber morphology on fiber buckling modes, fibers with various sections were deposited under different experimental conditions. The cross-sectional profiles (*e.g.* width and height) of the deposited fibers were firstly characterized by LSCM, then the substrates were relaxed to generate buckling (Fig. S3†). The solid marks in Fig. 3a are the experiment results of buckling, and the buckling mode changes with the variation of the height-to-width ratio H/W of the fibers. The red solid line $H = 0.65W$ divides the experiment results into two parts: (i) the left-top part represents in-surface buckling (green solid circles), and (ii) the right-bottom part represents out-of-surface buckling (blue solid

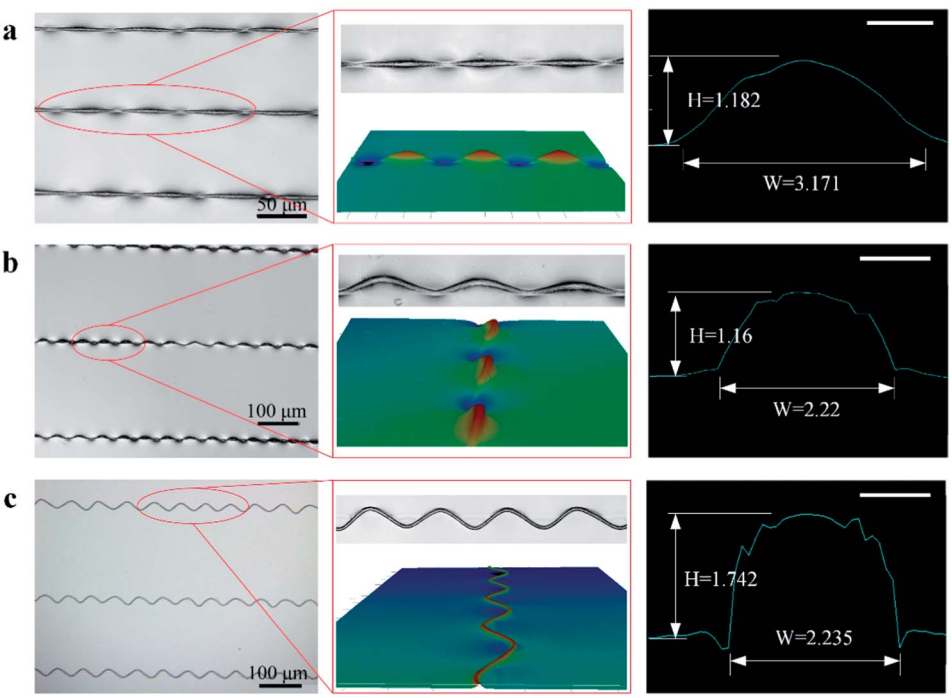

Fig. 2 Three typical buckling results of fibers deposited under different nozzle-to-collector distances. Sections (a), (b) and (c) represent normal-to-surface buckling, incline-to-surface buckling and in-surface buckling, respectively. The left column is LSCM images of the fibers, the middle column is 2D and 3D views of the left elliptical part. The right column represents typical cross-sections of the fibers in the left column and the default unit is micrometers. The scales bars in the right column represent 1 μm.

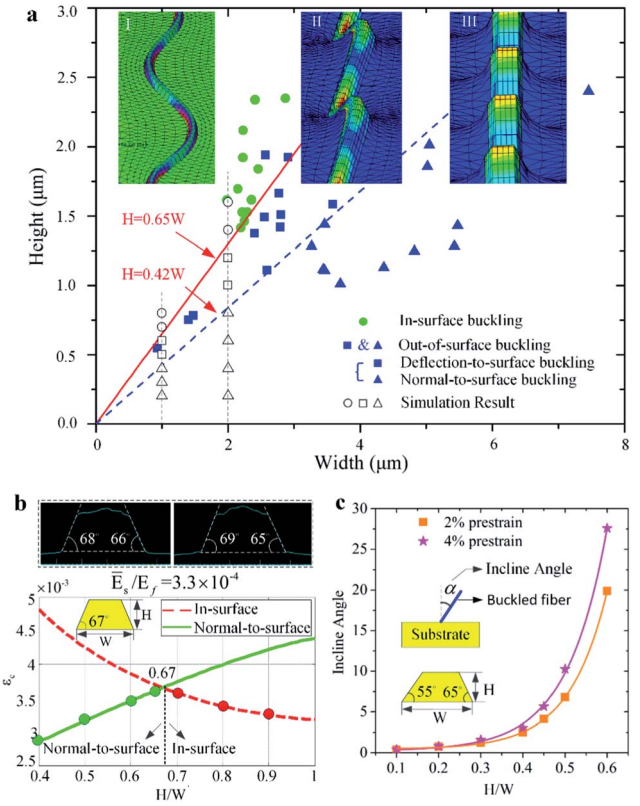

Fig. 3 Experimental and theoretical studies of buckled fibers on elastomeric substrates. (a) Influence of cross-sections on the buckling modes. The solid and hollow symbols represent experiment and FEA results, respectively. The (I), (II) and (III) in (a) are the FEA results of buckled fibers on substrates when the fiber width to height ratios are 0.7, 0.6 and 0.3, respectively (a trapezoid cross-section with interior angles of 65 and 55°). (b) Top are cross-sections of two fibers whose height-to-width ratio is close to the solid dividing line $H = 0.65W$, and bottom is the calculated critical buckling strain for fiber having such an isosceles trapezoid cross-section (the interior angle is 67°), where $\bar{E}_s/E_f = 3.3 \times 10^{-4}$ (the substrate modulus $E_s = 0.5$ Mpa, the fiber modulus $E_f = 2$ Gpa). The green and red dots denote out-of-surface and in-surface buckling under FEA when the height-to-width ratios (H/W) range from 0.4 to 0.6, and from 0.7 to 0.9, respectively. (c) Incline angles of buckled fibers *vs.* height-to-width ratio of fibers for a trapezoid cross-section (the interior angles are 65° and 55°) when $\bar{E}_s/E_f = 3.3 \times 10^{-4}$ ($E_s = 0.5$ Mpa, $E_f = 2$ Gpa).

squares and triangles). Additionally, out-of-surface buckling can be roughly divided into normal-to-surface buckling (blue solid triangles) and incline-to-surface buckling (blue solid squares), by the blue dash line $H = 0.42W$.

The mechanical model to distinguish out-of-surface buckling from in-surface buckling is critical for optimizing MES process parameters to generate non-wrinkled (in-surface buckled) fibers on the substrate. In our experiments, the dividing line between the two types of buckling is $H = 0.65W$. The buckling behavior of the fiber which has a static wavy configuration belongs to a classical mechanical problem that a thin, high-modulus layer on a semi-infinite low modulus support. The mechanisms of the two buckling modes can be discovered by the least-energy principle. For a given fiber-on-substrate system, the buckling mode with a lower total energy (including the bending energy due to fiber buckling, membrane energy in the fiber, and substrate energy in the substrate) is favorable. Basing on previous work,[34,35] we can get a more simplified function of the least total energy as (see ESI† for details) $U_{tot\_dir} = \frac{1}{2} E_f A \varepsilon_{c\_dir}(2\varepsilon_{pre} - \varepsilon_{c\_dir})$, where E_f and A mean the elastic modulus and sectional area of the fibers, ε_{pre} is the prestrain of the substrate, ε_{c_dir} (the subscript dir means in-/normal-to-surface direction) is the critical buckling strain or the minimum strain needed to induce buckling, *i.e.* the fiber only compresses when $\varepsilon_{pre} \leq \varepsilon_{c\_dir}$, and buckles when $\varepsilon_{pre} > \varepsilon_{c\_dir}$. By comparing the energies of the two buckling modes, we can derive that a buckling mode with a smaller critical buckling strain is favorable for having a smaller total energy. The critical buckling strain (see ESI† for details) is related to both the material properties ($\bar{E}_s/E_f$) and the cross-section of the fibers ($I_{insurface}$, I_{normal}, A, W). For a fiber on substrate, parameters like $\bar{E}_s/E_f$, A and W are independent of direction, so the moment of inertia of the fibers ($I_{insurface}$, I_{normal}) in different directions is the key to determining the buckling modes.

Top of Fig. 3b are the cross-sections of two fibers with height-to-width ratios close to the dividing line, and these fibers buckle out of surface and in surface, respectively. The sections of the fibers are complex, but they can be simplified as an isosceles trapezoid with an interior angle of 67°, then the moment of inertia is obtained as a function of the height-to-width ratio in in-surface/normal-to-surface direction ($I_{insurface}$, I_{normal}), and the critical buckling strain of the fiber is calculated (see ESI† for details). The critical point between in-/normal-to-surface buckling is ~0.67 as shown in Fig. 3b when the moduli of PVDF and PDMS are 2 Gpa and 0.5 Mpa, respectively. An isosceles trapezoid cross-section (67° interior angle) with different aspect ratios is simulated using commercial finite element analysis (FEA) software (Abaqus). Different buckling modes may appear when the height of the stiff layer increases gradually and the width (*i.e.*, the contact width between fiber and substrate) keeps constant at 2 μm. The FEA results predict that the change point is located between 0.65–0.7, which is in good agreement with the experimental change point 0.65 and the analytical change point 0.67. For other sections, such as rectangular and semi-elliptical, they are similar to a trapezoid, which has a critical point at in-/normal-to-surface buckling mode change (Fig. S6†). But for a cross-section which has equal bending stiffness in in-/normal-to-surface directions, such as circular, square and regular octagon, in-surface buckling mode is always energetically favorable for having lower critical buckling strain (Fig. S7†). The result is consistent with Ryu's experiment on silicon nanowires which have a regular hexagonal cross-section buckle only within the substrate surface.[15]

For an absolute symmetrical stiff layer or fiber on substrate, such as an isosceles trapezoid with an interior angle of 67°, the FEA results show that the incline angle of buckled fiber is approximately zero when the height-to-width ratio is 0.1–0.6, namely, only normal-to-surface buckling occurs. It is a challenge for electrohydrodynamic direct-writing to fabricate absolutely symmetric structures owing to the complicated

evaporation and solidification process. The height-to-width ratio and symmetrical characteristic are two coupled factors for buckling mode in addition to prestrain of the substrate. To validate the influence of symmetry, the buckling mode of the trapezoid sections with different interior angles (as example, 65 and 55°) and height-to-width ratios (from 0.1 to 0.6) are considered. The angle difference is 10° as the deviation of the interior angle is less than 15° in the measurement results. The incline angle α of the buckled fiber keeps a small value initially, and only normal-to-surface buckling is observed, then it increases sharply with the increase of the height-to-width ratio, and incline-to-surface buckling can be observed. The inflexion point of the height-to-width ratio is between 0.4–0.45 (simulated by Abaqus), which is in good agreement with the experiment result of $H = 0.42W$. Additionally, we find that the prestrain of the substrate is of importance to the incline angle that the incline angle increases with the prestrain. The buckling mechanism further confirms that traditional film-on-substrate is absolutely normal-to-surface buckling, not incline-to-surface buckling. In some reported works, the aspect ratio $H/W \ll 0.1$ (Si ribbon with width 5 to 50 μm and thickness 20 to 320 nm[33] or Si ribbon with width 2 to 200 μm and thickness 100 nm[36]), so only normal-to-surface buckling occurs. Based on the analysis above, the three buckling modes can be totally controlled by the fiber cross-section which is determined by the MES parameters.

The buckling wavelength, amplitude and phase of the fibers are also key parameters to actual stretchability and application. Fig. 4a shows the influence of prestrain on the wave shape that the buckling wavelength decreases and the amplitude increases with the prestrain of the substrate. When the prestrain increases from 20 to 80%, the buckling wave becomes increasingly compact, and the ratio of amplitude to wavelength changes from 0.3 to 0.62. Additionally, the phase of the buckled fibers determines the uniformity and integration of the buckled fiber-array. For two identical fibers on the same prestrained substrate but far apart from each other, they will form a wave-shaped structure with the same wavelength and amplitude, but the wave phase is hard to synchronize. The experiment showed the spacing plays an important role in buckle synchronization, and it also has been proven in theory.[36] Mechanical interactions in the underlying PDMS substrate become significant when the gap decreases, so the phase synchronization can be tuned by the spacing, and large scale in-surface buckled fiber-array with high uniformity and integration can be fabricated. In-surface buckled fiber is able to be conformal to the substrate surface before and after deformation without out-of-surface wrinkling and warping (Fig. S4†), which benefits the encapsulation, device performance and lifetime.

MES process can electrospin and position PVDF fibers over a large area with low cost and high efficiency. The electrospun PVDF fiber has high piezoelectricity even without post-processing such as high electrical field.[30,37] Whether the buckled PVDF fiber still has a piezoelectric response is of importance to a highly stretchable generator and sensor application. Stretchable piezoelectric devices made up of in-surface buckled fibers are fabricated and tested as Fig. 5a shows. The stretchable piezoelectric device is fixed on a home-made tensile platform, the buckled fiber-array is connected to probes through metallic electrodes. When the tensile platform reciprocates, the piezoelectric PVDF fibers generate a current or voltage which is characterized by the semiconductor characterization system.

Fig. 5b shows the current (~1.2 nA) and voltage (~40 mV) measured from a stretchable piezoelectric device (3 cm long between electrodes) consisting of about 120 direct-written in-surface buckled PVDF fibers under periodic stretch and release (30% strain, 0.5 Hz), which demonstrates both high stretchability and high piezoelectricity of the fibers. The voltage and current measured in Fig. 5b have opposite signs (from up to bottom, the ordinate of voltage is from negative to positive,

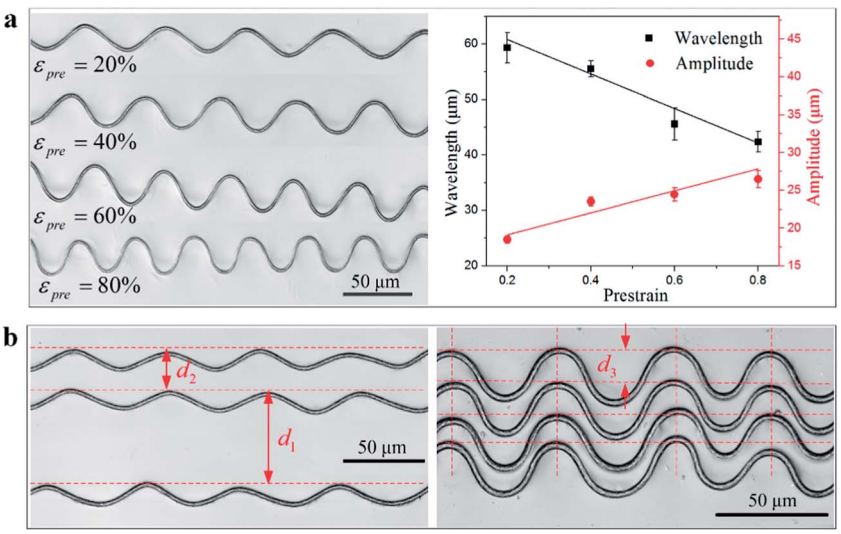

Fig. 4 (a) The left panel shows images of in-surface buckled fibers for various prestrain levels (ε_{pre}). The right panel shows the wavelength and amplitude of the buckles *vs.* prestrains. (b) Influence of spacing on the conformance of in-surface buckling.

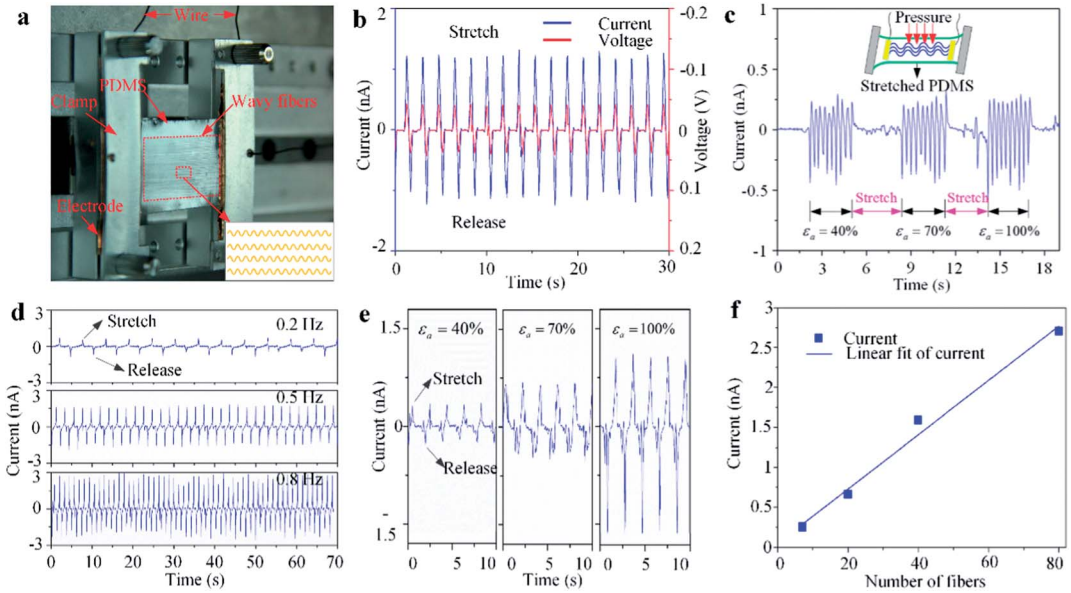

Fig. 5 Response of the stretchable piezoelectric devices. (a) Photograph of the tensile test platform. (b) Output current and voltage of the device consisting of 120 PVDF fibers measured with respect to time under an applied strain of 30% at 0.5 Hz. (c) Piezoelectric behavior of in-surface buckled fibers on PDMS substrate under constant periodic pressure while with different applied strains. Sections (d), (e) and (f) reveal the device performance with respect to frequency (40 fibers, 70%), strain (20 fibers, 0.5 Hz) and number of fibers (70%, 0.5 Hz).

while it is opposite for the current), because the current flows through the PVDF fibers (like current flows through a battery) is from low to high potential. The electrical output of the energy provider is mainly affected by the strain rate (the rate of strain change versus time) and the number of fibers in the device. The strain rate is relevant to the stretch-and-release cycle frequency and amplitude (applied strain ε_a). So there are three approaches to enhancing the output current significantly. (i) *Increasing the frequency.* From top to bottom of Fig. 5d, the average maximum currents are 0.65, 1.62 and 2.8 nA, corresponding to frequencies of 0.2, 0.5, and 0.8 Hz, respectively (40 fibers, ε_a = 70%). (ii) *Increasing the applied strain.* From left to right of Fig. 5e, the strains of the stretch-release test are 40, 70 and 100%, and the output current increases from 0.33 to 1.1 nA (20 fibers, 0.5 Hz). The output current increases with the frequency and the applied strain, while they remain approximately constant during the same stretch and release test. (iii) *Increasing the number of fibers.* It can be seen from Fig. 5f that the output current increases linearly with the number of fibers. A stretchable piezoelectric generator with an accurate output current can be fabricated since MES is able to manipulate fibers individually. These results show that the performance characteristics of buckled piezoelectric PVDF fibers are consistent with the fundamental piezoelectric theory $i = d_{33}EA\dot{\varepsilon}$,[38] where i is the generated current, d_{33} is the piezoelectric charge constant, E is Young's modulus, the cross-sectional area A is proportional to the number of fibers, and the applied strain rate $\dot{\varepsilon}$ is proportional to the stretch frequency under a specific applied strain, or the applied strain under a specific frequency. When more PVDF fibers are integrated into one device with large strain and frequency, the response current is larger (~50 nA for 120 fibers under 100% strain at 4 Hz). This device can also work as a stretchable pressure sensor under progressive tensions as shown in Fig. 5c. When the device is stretched by different applied strains, its sensitivity to pressure is maintained ideally, owing to the in-surface buckled fibers. This characteristic can be used in artificial skin which can measure pressure accurately under different tensions. It should be emphasized that buckled PVDF fibers on elastomeric substrates can be stretched over 100% applied strain (limited by the failure of PDMS), much larger than the strain of the reported piezoelectric generator or sensor (8% stretchability in ref. 7).

Conclusions

In summary, stretchable nanogenerators with highly uniform, controllable buckled fiber arrays are directly written onto pre-strained elastomeric substrate by using MES. The process realizes direct-writing of the PVDF fiber and obtaining piezoactive β phase in one step, without further processing such as transfer printing and electrical poling. By individual manipulating single fiber (such as the number, position and morphology), synchronized in-surface buckled fibers with the same phase, wavelength and amplitude are obtained. A stretchable piezoelectric generator exhibits an excellent response at an extremely large applied strain. Additionally, a stretchable pressure sensor with in-surface buckled fiber array shows the stable pressure measurement under various applied strains owing to its in-surface deformation. The collective results suggest that stretchable piezoelectric generators and sensors can be fabricated by cost-effective electrohydrodynamic direct-writing, with high piezoelectric response, attractive stretchability and potential to be integrated into stretchable electronics such as human monitoring and artificial skin.

Acknowledgements

The authors acknowledge support from the National Natural Science Foundation of China (51322507, 51035002, 51121002) and New Century Excellent Talents in University (NCET-11-0171). The general characterization facilities were provided through the National Laboratory.

References

1 S. C. Mannsfeld, B. C. Tee, R. M. Stoltenberg, C. V. H. Chen, S. Barman, B. V. Muir, A. N. Sokolov, C. Reese and Z. Bao, *Nat. Mater.*, 2010, **9**, 859–864.
2 K. Takei, T. Takahashi, J. C. Ho, H. Ko, A. G. Gillies, P. W. Leu, R. S. Fearing and A. Javey, *Nat. Mater.*, 2010, **9**, 821–826.
3 D. H. Kim, N. Lu, R. Ma, Y.-S. Kim, R.-H. Kim, S. Wang, J. Wu, S. M. Won, H. Tao and A. Islam, *Science*, 2011, **333**, 838–843.
4 T. Yamada, Y. Hayamizu, Y. Yamamoto, Y. Yomogida, A. Izadi-Najafabadi, D. N. Futaba and K. Hata, *Nat. Nanotechnol.*, 2011, **6**, 296–301.
5 H. C. Ko, M. P. Stoykovich, J. Z. Song, V. Malyarchuk, W. M. Choi, C. J. Yu, J. B. Geddes, J. L. Xiao, S. D. Wang, Y. G. Huang and J. A. Rogers, *Nature*, 2008, **454**, 748–753.
6 S. Xu, Y. Zhang, J. Cho, J. Lee, X. Huang, L. Jia, J. A. Fan, Y. Su, J. Su and H. Zhang, *Nat. Commun.*, 2013, **4**, 1543.
7 Y. Qi, J. Kim, T. D. Nguyen, B. Lisko, P. K. Purohit and M. C. McAlpine, *Nano Lett.*, 2011, **11**, 1331–1336.
8 P. Lee, J. Lee, H. Lee, J. Yeo, S. Hong, K. H. Nam, D. Lee, S. S. Lee and S. H. Ko, *Adv. Mater.*, 2012, **24**, 3326–3332.
9 J. Lee, P. Lee, H. Lee, D. Lee, S. S. Lee and S. H. Ko, *Nanoscale*, 2012, **4**, 6408–6414.
10 D. H. Kim, J. Xiao, J. Song, Y. Huang and J. A. Rogers, *Adv. Mater.*, 2010, **22**, 2108–2124.
11 Y. Su, J. Wu, Z. Fan, K.-C. Hwang, J. Song, Y. Huang and J. A. Rogers, *J. Mech. Phys. Solids*, 2012, **60**, 487–508.
12 Y. Wang, R. Yang, Z. Shi, L. Zhang, D. Shi, E. Wang and G. Zhang, *ACS Nano*, 2011, **5**, 3645–3650.
13 Y. Zhang, S. Xu, H. Fu, J. Lee, J. Su, K.-C. Hwang, J. A. Rogers and Y. Huang, *Soft Matter*, 2013, **9**, 8062–8070.
14 M. Gonzalez, F. Axisa, M. V. Bulcke, D. Brosteaux, B. Vandevelde and J. Vanfleteren, *Microelectron. Reliab.*, 2008, **48**, 825–832.
15 S. Y. Ryu, J. L. Xiao, W. Il Park, K. S. Son, Y. Y. Huang, U. Paik and J. A. Rogers, *Nano Lett.*, 2009, **9**, 3214–3219.
16 F. Xu, W. Lu and Y. Zhu, *ACS Nano*, 2010, **5**, 672–678.
17 Y. Zhu and F. Xu, *Adv. Mater.*, 2012, **24**, 1073–1077.
18 A. J. Baca, J. H. Ahn, Y. G. Sun, M. A. Meitl, E. Menard, H. S. Kim, W. M. Choi, D. H. Kim, Y. Huang and J. A. Rogers, *Angew. Chem., Int. Ed.*, 2008, **47**, 5524–5542.
19 A. Shirinov and W. Schomburg, *Sens. Actuators, A*, 2008, **142**, 48–55.
20 J. G. Rocha, L. M. Goncalves, P. Rocha, M. Silva and S. Lanceros-Mendez, *IEEE Trans. Ind. Electron.*, 2010, **57**, 813–819.
21 T. Ma, Y. Wang, R. Tang, H. Yu and H. Jiang, *J. Appl. Phys.*, 2013, **113**, 204503.
22 L. Persano, C. Dagdeviren, Y. Su, Y. Zhang, S. Girardo, D. Pisignano, Y. Huang and J. A. Rogers, *Nat. Commun.*, 2013, **4**, 1633.
23 B. J. Hansen, Y. Liu, R. Yang and Z. L. Wang, *ACS Nano*, 2010, **4**, 3647–3652.
24 N. Bu, Y. Huang, X. Wang and Z. Yin, *Mater. Manuf. Processes*, 2012, **27**, 1318–1323.
25 Y. Huang, X. Wang, Y. Duan, N. Bu and Z. Yin, *Soft Matter*, 2012, **8**, 8302–8311.
26 D. H. Sun, C. Chang, S. Li and L. W. Lin, *Nano Lett.*, 2006, **6**, 839–842.
27 D. H. Reneker and A. L. Yarin, *Polymer*, 2008, **49**, 2387–2425.
28 S.-Y. Min, T.-S. Kim, B. J. Kim, H. Cho, Y.-Y. Noh, H. Yang, J. H. Cho and T.-W. Lee, *Nat. Commun.*, 2013, **4**, 1773.
29 Y. Huang, N. Bu, Y. Duan, Y. Pan, H. Liu, Z. Yin and Y. Xiong, *Nanoscale*, 2013, **5**, 12007–12017.
30 C. Chang, V. H. Tran, J. Wang, Y.-K. Fuh and L. Lin, *Nano Lett.*, 2010, **10**, 726–731.
31 T. Han, D. H. Reneker and A. L. Yarin, *Polymer*, 2008, **49**, 2160–2169.
32 Z. P. Yin, Y. A. Huang, N. B. Bu, X. M. Wang and Y. L. Xiong, *Chin. Sci. Bull.*, 2010, **55**, 3383–3407.
33 D. Y. Khang, H. Q. Jiang, Y. Huang and J. A. Rogers, *Science*, 2006, **311**, 208–212.
34 J. Xiao, H. Jiang, D. Y. Khang, J. Wu, Y. Huang and J. A. Rogers, *J. Appl. Phys.*, 2008, **104**, 033543.
35 J. Xiao, S. Y. Ryu, Y. Huang, K. C. Hwang, U. Paik and J. A. Rogers, *Nanotechnology*, 2010, **21**, 085708.
36 H. Jiang, D.-Y. Khang, H. Fei, H. Kim, Y. Huang, J. Xiao and J. A. Rogers, *J. Mech. Phys. Solids*, 2008, **56**, 2585–2598.
37 J. Pu, X. Yan, Y. Jiang, C. Chang and L. Lin, *Sens. Actuators, A*, 2010, **164**, 131–136.
38 J. Sirohi and I. Chopra, *J. Intell. Mater. Syst. Struct.*, 2000, **11**, 246–257.